Generation of diurnal K_1 internal tide in the Luzon Strait and its influence on surface tide in the South China Sea

Sen Jan,[1,4] Ching-Sheng Chern,[2,4] Joe Wang,[2,4] and Shenn-Yu Chao[3]

[1]   The predominance of diurnal surface tides over semidiurnal surface tides in the South China Sea (SCS) has been attributed to the near-resonance response of the former in the SCS. Recent observations further revealed vigorous internal tides in the northern SCS. Conceivably, internal tides generated in the Luzon Strait could modify the surface tide in the SCS. We use a three-dimensional tide model of the East Asian seas to address this issue. With a typical summertime stratification of the SCS as the initial condition, energy budget indicates that one third of the incident K_1 surface tide energy is converted to the baroclinic energy over topographic ridges in the Luzon Strait. In comparison with a global tidal model [Matsumoto et al., 2000], our numerical experiments that annihilated or reduced the K_1 internal tide in the Luzon Strait led to up to 50% amplification of the simulated K_1 surface tide in the SCS. This suggests that the baroclinic energy conversion substantially reduces the amplitude of K_1 surface tide in the SCS. The simulated phases in the SCS differ little from those calculated from Matsumoto's tide model, suggesting that the modification is primarily on the amplitude. Two-dimensional surface tidal models lack baroclinic energy conversion in the Luzon Strait; the consequent overestimation of surface K_1 tide can be reduced only through precise prescription of sea levels in the Luzon Strait or assimilation of sea level data.

1.   Introduction

[2]   The South China Sea (SCS), covering an area of about 3.5×10^6 km^2, is a semienclosed basin with depths of 3000–4000 m in the central basin and less than 200 m over most of peripheral shelves (Figure 1). There are five major passages connecting the SCS to surrounding seas. Both the Taiwan and Karimata straits are shallow passages (depth <100 m) to the East China Sea and the Java Sea, respectively. The Mindoro and Balabac straits are narrow passages to the Sulu Sea with limited water exchange. Among all passages, the Luzon Strait is the deepest and also the most important one connecting the SCS to the northwest Pacific Ocean.

[3]   It is well known that the barotropic tides in the SCS are dominated by diurnal constituents [*Ye and Robinson*, 1983; *Huang et al.*, 1994; *Mazzega and Berge*, 1994; *Yanagi et al.*, 1997]. Using a two-dimensional tide model, *Yanagi and Takao* [1998] verified that the quarter-wave resonant response of diurnal tides leads to the predomi-

nance. The cotidal chart plotted using harmonic constants derived from a two-dimensional global tide model with sea level data assimilation [*Matsumoto et al.*, 2000, hereafter referred to as NAO.99] illustrates that the diurnal K_1 tide with amplitude of about 20 cm propagates southwestward from the Pacific Ocean to the SCS mainly through the Luzon Strait (Figure 2a). The southwestward-propagating K_1 tide further amplifies to 40 cm over the deep basin of the SCS. The K_1 tide is greatly amplified near heads of the Gulf of Tonkin and the Gulf of Thailand due to the near-resonance diurnal response of the two gulfs [*Fang et al.*, 1999]. By comparison, the semidiurnal M_2 tide entering through the Luzon Strait behaves as a decaying wave while propagating southwestward in the SCS. Its amplitude drops rapidly from 40 to 20 cm while passing through the Luzon Strait and further reduces to 10–20 cm in the central basin of the SCS [*Ye and Robinson*, 1983; *Huang et al.*, 1994; *Fang et al.*, 1999].
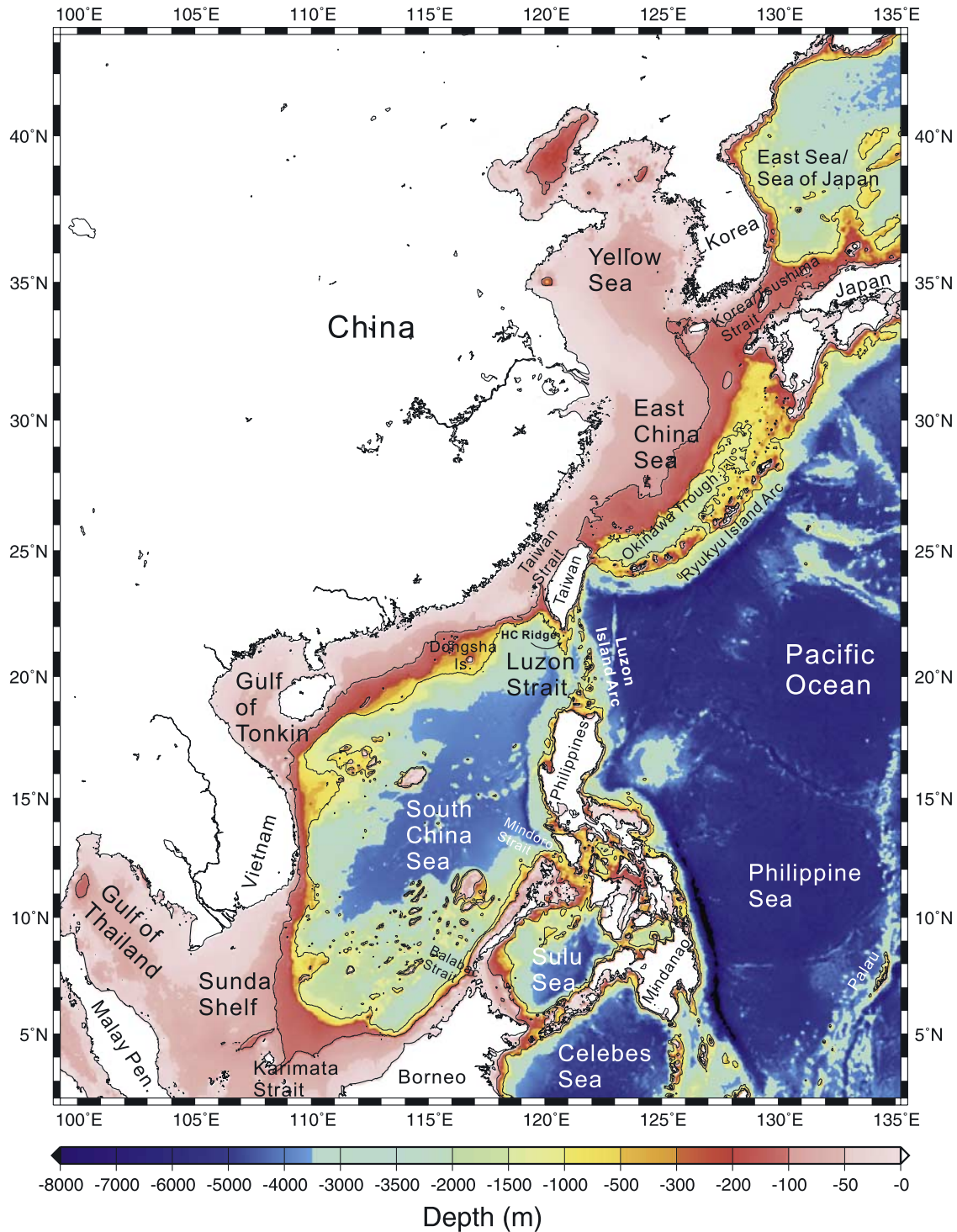
[4]   Recently, dramatic internal tides and solitary waves and bores with vertical isotherm displacements up to 100 m were observed near the Dongsha Island in the northern SCS [*Lynch et al.*, 2004; *Duda et al.*, 2004; *Ramp et al.*, 2004]. Using a three-dimensional tide model, *Niwa and Hibiya* [2004] confirmed that the continental shelf/slope of the East China Sea and the prominent topographic ridges in the Luzon Strait are the major generation sites of the M_2 internal tides in the northwest Pacific Ocean. They estimated that 25% of the M_2 barotropic tide energy was converted to baroclinic energy in the Luzon Strait.

[1]Institute of Hydrological Sciences, National Central University, Jung-li, Taiwan, Republic of China.
[2]Institute of Oceanography, National Taiwan University, Taipei, Taiwan, Republic of China.
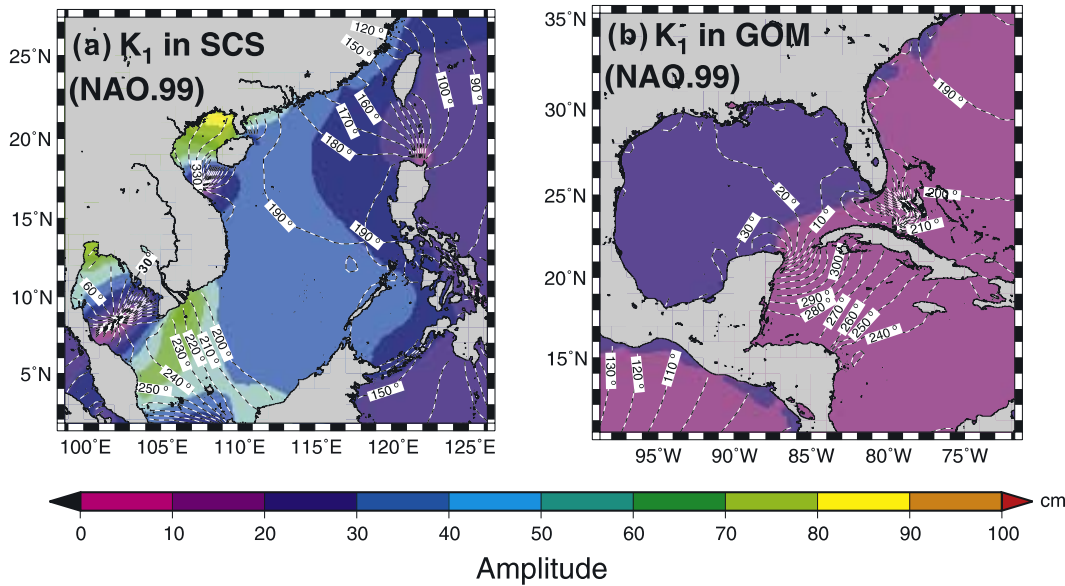[3]Horn Point Laboratory, University of Maryland Center for Environmental Science, Cambridge, MD, USA.
[4]National Center for Ocean Research, Taipei, Taiwan, Republic of China.

Figure 1. Bathymetry of our three-dimensional model domain, including the East Asian seas and northwest Pacific Ocean. HC ridge represents the Heng-Chun Ridge extended from southernmost of Taiwan Island.

[5] Of interest are the similarity and dissimilarity between the Gulf of Mexico (GOM) and the SCS. The GOM is also semienclosed with passages to the Atlantic Ocean and the Caribbean Sea. Tides in the GOM are also predominantly diurnal rather than semidiurnal [*Reid and Whitaker*, 1981]. The amplitude of K_1 tide is about 10 cm in the entrance of the GOM but increases to about 20 cm in the entire GOM (Figure 2b). The amplification and predominance of the diurnal tide are attributed to the cooscillating tide response in the GOM [*Zetler and Hansen*, 1971]. The baroclinic tides, on the other hand, are seasonally modulated and are an order of magnitude smaller than the barotropic tides [*He and Weisberg*, 2002]. Not surprisingly, *Clarke* [1991] con-

Figure 2. Harmonic constants (amplitude and phase) of K$_1$ tide in the (a) South China Sea and the (b) Gulf of Mexico according to *Matsumoto et al.* [2000].

cluded that the effects of baroclinic tides on the deterministic barotropic tides are negligible in the GOM.

[6] In contrast, internal tides in the SCS are remarkably strong and may modify surface tides. The internal tides are being investigated extensively, but how they modify the surface tide is not clear. Previous barotropic tide studies using two-dimensional models mostly concentrated on the accuracy of modeled sea levels [e.g., *Fang et al.*, 1999]. Recent three-dimensional numerical studies focused primarily on the generation, energetics, and evolution of the semidiurnal M$_2$ internal tide in the Luzon Strait and northern SCS [e.g., *Niwa and Hibiya*, 2004]; the investigation on the diurnal tides was scarce. To investigate the potential influence of the diurnal internal tide created in the Luzon Strait on the characteristic of the surface tide in the SCS, we adopt a process-oriented numerical approach below. A three-dimensional tide model is used to simulate the K$_1$ barotropic and baroclinic tides in the East Asian seas. Harmonic constants analyzed from the model results are compared with those of NAO.99. Subsequent numerical experiments evaluate the modification of surface tide in response to the generation of internal tide in the Luzon Strait. The importance of topographic ridges in the Luzon Strait in generating internal tides is also investigated. For simplicity, we concentrate on the simulation of the major diurnal constituent, the K$_1$.

2. Model Description

[7] Our tide model is a modified version of the Princeton Ocean Model which was described in the work of *Blumberg and Mellor* [1987]. The model is a three-dimensional, nonlinear, primitive equation model with Boussinesq and hydrostatic approximations. We have added tidal forcing to facilitate this study. The vertical axis is transformed to the σ coordinate by $\sigma = (z - \eta)/(H + \eta)$, where z is positive upward with the origin placed at the mean sea level, η is the

sea level fluctuation, and H is the mean water depth. The governing equations are as follows:

$$\frac{\partial UD}{\partial t} + ADV_U - fVD = -GRAD_x P' + DIF_U$$
$$+ gD \frac{\partial(\zeta - \beta\eta)}{\partial x} - r(U - \bar{U})D \qquad (1)$$

$$\frac{\partial VD}{\partial t} + ADV_V + fUD = -GRAD_y P' + DIF_V$$
$$+ gD \frac{\partial(\zeta - \beta\eta)}{\partial y} - r(V - \bar{V})D \qquad (2)$$

$$\frac{\partial P'}{\partial \sigma} = -\rho' gD \qquad (3)$$

$$\frac{\partial \eta}{\partial t} + \frac{\partial UD}{\partial x} + \frac{\partial VD}{\partial y} + \frac{\partial w}{\partial \sigma} = 0 \qquad (4)$$

$$\frac{\partial \varphi D}{\partial t} + ADV_\varphi = DIF_\varphi \qquad (5)$$

where (U, V) are the horizontal velocity components in the x and y directions; w is the velocity component normal to σ surface; D is the total water depth ($D = H + \eta$); t is the time; f is the Coriolis parameter; ρ' is the perturbation density; P' is the perturbation pressure; (ADV_U, ADV_V), $(GRAD_x P', GRAD_y P')$, and (DIF_U, DIF_V) are the advection, pressure gradient, and diffusion terms, respectively, in the horizontal momentum equations (Mellor data available at http://www.aos.princeton.edu/WWWPUBLIC/htdocs.pom); β (= 0.94 for K$_1$ tide) represents the loading effect due to ocean tides [*Foreman et al.*, 1993]; g is the gravitational

Table 1. Model Specification

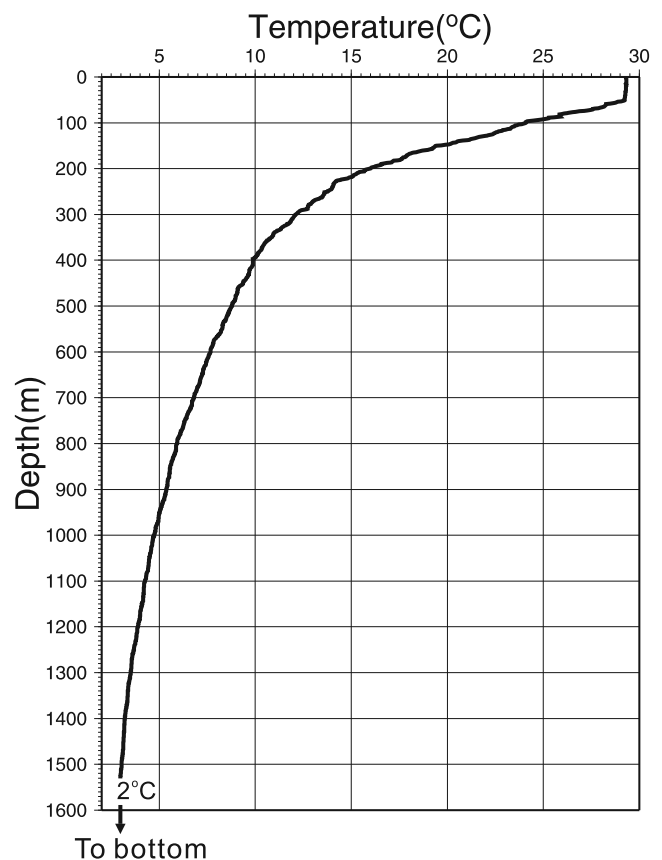| Parameter	Specification
Range of domain	$99.25°-135.25°E$ and $2.25°-43.25°N$ (Figure 1)
Horizontal resolution	$1/12°$ ($\sim$9.17 km near equator)
Vertical resolution	51 σ layer with uneven σ spacing ($-\sigma_k = 0$, 0.002, 0.004, 0.006, 0.008, 0.01, 0.012, 0.014, 0.018, 0.022, 0.026, 0.03, 0.034, 0.037, 0.045, 0.053, 0.061, 0.069, 0.077, 0.085, 0.1, 0.116, 0.132, 0.148, 0.179, 0.211, 0.243, 0.274, 0.306, 0.337, 0.369, 0.4, 0.432, 0.464, 0.495, 0.527, 0.558, 0.59, 0.621, 0.653, 0.684, 0.716, 0.748, 0.779, 0.811, 0.842, 0.874, 0.905, 0.937, 0.968, and 1 as k varies from 1 to 51)
Topography (depths)	(1) 1-min depth archive in the region between $105°-135°E$ and $2°-35°N$, and (2) 2-min gridded global depths database ETOPO2 (U.S. Department of Commerce, National Oceanic and Atmospheric Administration, National Geophysical Data Center data available at http://www.ngdc.noaa.gov/mgg/fliers/01mgg04.html) elsewhere
Adjusted equilibrium tides in equations (1) and (2)	$\zeta = f_{K_1} H_{K_1} \cos[\bar{\omega}_{K_1} t + (V_0 + \mu) + \lambda]$, where f_{K_1} is nodal factor, ω_{K_1} is K_1 tidal frequency, V_0 is initial phase angle of the equilibrium tides, μ is nodal angle, λ is longitude, and $H_{K_1} = 0.104\ \sin 2\phi$ for K_1 tide (ϕ: latitude)
Horizontal viscosity and diffusivity	*Smagorinsky's* [1963] formulation
Vertical viscosity and diffusivity	*Mellor and Yamada's* [1982] level 2.5 turbulence closure scheme
Bottom stress	$C_z[U^2 + V^2]^{0.5}(U, V)$, where $C_z = \text{MAX}[\kappa^2/\{\ln[(1 + \sigma_{50})H/z_0]\}^2, 0.0025]$ ($\kappa = 0.4$ is the von Karman constant, and $z_0 = 0.01$ m is the bottom roughness length)

acceleration; $(\bar{U}, \bar{V})$ represent depth-averaged horizontal velocities; φ can be the temperature (T) or salinity (S); and ADV_φ and DIF_φ are the advection and diffusion terms, respectively, in temperature and salinity equations. The nonlinear interactions between internal tides and internal waves are parameterized by linear damping terms $-r(U - \bar{U})$ and $-r(V - \bar{V})$ in equations (1) and (2), respectively, where r is a damping coefficient which is set to 0.2 day^{-1} as suggested by *Niwa and Hibiya* [2001, 2004]. The adjusted height of equilibrium tides (ζ) is calculated using the formulation described in the study of *Pugh* [1987] (see Table 1 for details). Table 1 summarizes major specifications for the model.

[8] The initially motionless ocean has horizontally homogeneous but vertically stratified temperature field. Figure 3 shows the initial temperature profile which was obtained by *Chen et al.* [2006] at a station in the northern SCS (118.5°E, 19°N) in July 1999. Salinity is assumed to be homogeneous because it varies vertically by less than 3% in deep reaches of the SCS where the density stratification is dominated by the vertical temperature variation. Subsequently, the model is driven by prescribed tidal sea levels on all open ocean boundaries through a forced radiation condition similar to that adopted by *Blumberg and Kantha* [1985]. The tidal sea levels on the open boundaries are computed using the harmonic constants of NAO.99. The depth-averaged tidal current velocity normal to the open boundaries is determined by the following equation:

$$u_{nB} = u_{2D} + C\left(\eta_B - \eta_{pre}\right)/H \qquad (6)$$

where $\boldsymbol{u}_{2D}$ is calculated from a fine-tuned, two-dimensional tide model of *Jan et al.* [2004], $C(= \sqrt{gH})$ is the phase speed of a shallow water gravity wave, η_B is the sea level calculated by the three-dimensional tidal model, and η_{pre} is the prescribed tidal sea level on open boundaries. A flow relaxation scheme described by *Engedahl* [1995] is applied to the internal mode velocity and temperature in a 1° wide strip adjacent to open boundaries to eliminate artificial reflections.

[9] It takes 8–10 days for the first vertical mode of internal tide to propagate from the source to open boundaries of the model. The basic model run is therefore set to 15 days. Hourly model results of the last three tidal cycles of K_1 tide are analyzed subsequently. To retain the dynamics of tidal waves as much as possible, the control run neither fine-tunes the model parameters nor assimilates the

Figure 3. Typical temperature profile of the SCS in summer. Data were obtained at (118.5°E, 19°N) in July 1999 by *Chen et al.* [2006].

observed sea levels into the model interior to improve accuracy.

3. Results

3.1. Barotropic Tide

[10] Figure 4 illustrates the cotidal chart and depth-averaged tidal current ellipses of the simulated K$_1$ barotropic tide in the SCS. The simulated cotidal patterns capture essential features of K$_1$ tide presented in earlier model results [*Yanagi and Takao*, 1998; *Fang et al.*, 1999; *Matsumoto et al.*, 2000]. The cophase distribution indicates that incident waves from the northwest Pacific propagate into the SCS through the Taiwan and Luzon straits and subsequently enter the Gulf of Tonkin and Gulf of Thailand. The amplitude in the central SCS is twofold of that in the northwest Pacific Ocean. Comparing to the harmonic constants of NAO.99, the amplitudes are about 20 cm overestimated between Vietnam and Malay Peninsula; the phases lag NAO.99 by approximately 10° in the central SCS but lead NAO.99 by 10° over the Sunda Shelf (cf. Figure 2a). The phase discrepancy suggests that the simulated surface tide propagates slower than that from NAO.99 in the central SCS. In consequence, the simulated tidal wave has to speed up over the Sunda Shelf to meet the prescribed tidal phase across the southern open boundary. In addition, the different levels of topographic representation between our model and NAO.99 and the emergence of internal tides in our model may also contribute to the phase discrepancy. The root mean square difference between our model and NAO.99 results is 3.2 cm for tidal sea levels in regions deeper than 1000 m. Notably, sinuous oscillations of the cophase line around the Luzon Strait and northern SCS are possibly caused by the internal tide because their length scale is comparable to the horizontal wavelength of the K$_1$ internal tide.

[11] Figure 4b shows relatively weaker tidal currents in the northwest Pacific Ocean and the main portion of the SCS. Tidal currents strengthen in the Luzon Strait (20−50 cm/s), the Gulfs of Tonkin and Thailand (∼50 cm/s), and the Sunda Shelf (∼20 cm/s). Moving eastward over the Sunda Shelf, the tidal amplitudes increase but tidal currents decrease considerably in the region from the southern tip of Vietnam to the West Coast of Malay Peninsula. This is indicative of an antinodal band for a standing wave. In contrast, smaller amplitudes and stronger tidal currents in the Luzon Strait are indicative of a nodal band.

[12] We also compared simulated barotropic tidal currents with observations conducted under the Asian Seas International Acoustics Experiment (ASIAEX) near the Dongsha Island [see *Lynch et al.*, 2004 for an overview of the project]. Figure 5 shows the depth-averaged tidal current ellipses from our model results and corresponding ones observed at five acoustic Doppler current profiler (ADCP) stations of ASIAEX [Table 5 in the paper of *Beardsley et al.*, 2004]. Locations of the five ADCP stations are marked in the right panel of Figure 5. On average, the modeled barotropic tidal currents are about 15% stronger than those observed. Discrepancies between the simulated and observed major tidal axis orientation are less than 10°. The truncation error of local topographic structure is likely a major source causing the discrepancy. Further fine-tuning without better topography resolution may further improve the model performance in this locale, but it may not serve the major interest of this basin-wide process-oriented study.
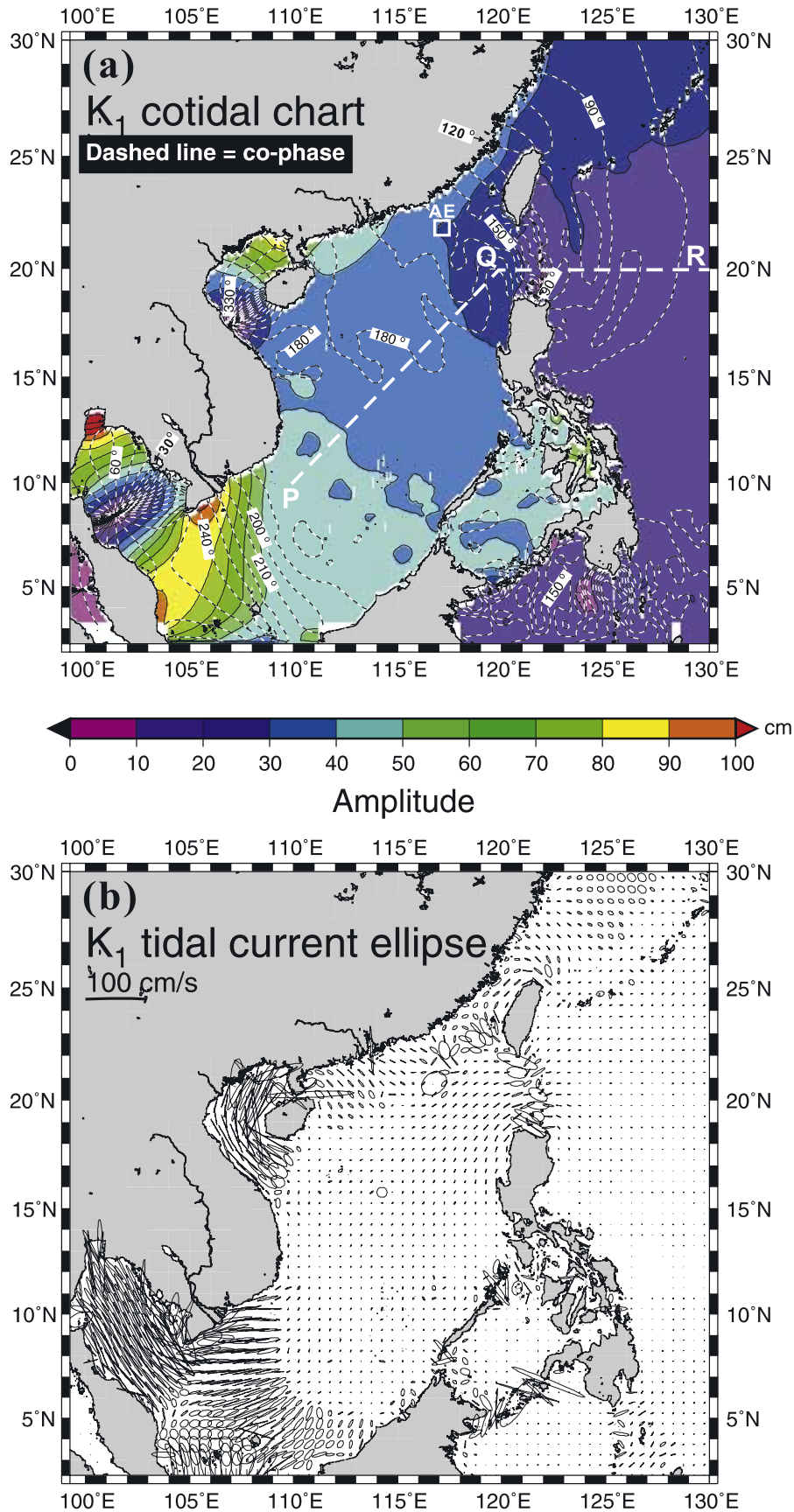
3.2. Baroclinic Tide

[13] Figure 6 shows instantaneous sea surface elevations and vertical isopycnal displacements relative to 150 m depth at days 14 and 14.5. The tidal phase difference between the two instants is approximately 180°. The surface elevations in the SCS and the northwest Pacific Ocean are nearly out of phase by 180°. The vertical isopycnal displacement indicates pronounced internal tides in the northwest Pacific Ocean (between 24° and 16°N) and the northern SCS. The horizontal internal tide pattern is complex in the southern SCS due to the interference with reflection waves from the Sunda Shelf. The vertical density (σ_t) distribution and the bottom depth contour along 20°N in Figure 7a demonstrate that the isopycnal excursion (twofold of the internal tide amplitude) is larger than 45 m immediately west of the Hengchun Ridge, about 20 m just east of the Dongsha Island and 10−20 m on the Pacific side of Luzon Strait. The Luzon Strait seems to be the center of action, as oscillations decrease in amplitude with distance away from it. The corresponding excursions near Dongsha Island during ASIAEX, after harmonic analysis, were ∼10 m in neap tide and ∼50 m in spring tide [*Duda et al.*, 2004]. Thus the modeled excursion appears to be reasonable even though we adopt the hydrostatic approximation and include only the K$_1$ tide. Note that an observed vertical isotherm excursion of more than 100 m in the northern SCS [*Ramp et al.*, 2004] is normally a mixture of internal tides, nonlinear internal waves, and solitary waves and bores, of which the last three are mostly excluded by our hydrostatic model.

[14] The horizontal wavelength of the internal tide, estimated by the distance between two successive wave crests (or troughs) in Figure 6, is about 400 km in the Pacific Ocean around 20°N, 300−350 km in the northern SCS, and 240 km in the southern SCS. Changing water depths (∼5000 m in the northwest Pacific, ∼3000 m in the northern SCS, and ∼1500 m in the southern SCS) are mostly responsible for the difference. The corresponding propagation speed (wavelength divided by K$_1$ tide period) is 4.6 m/s in the Pacific Ocean, 3.4−4.0 m/s in the northern SCS, and 2.8 m/s in the southern SCS. These estimates are consistent with phase speeds of the first baroclinic mode.
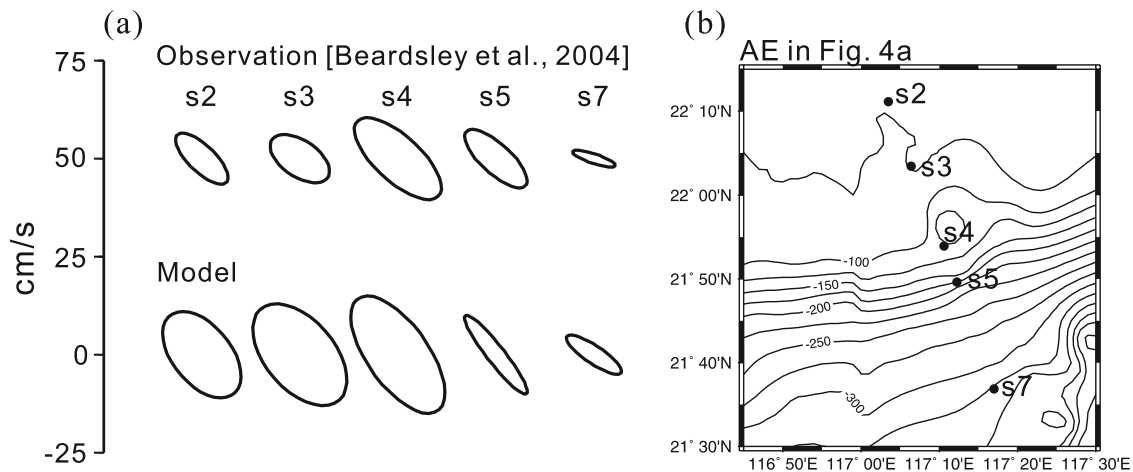
[15] Relative to waves generated in the Luzon Strait, Figure 6 also reveals shorter internal tide wavelengths (100−150 km) in the Celebes Sea and the Pacific Ocean south of 10°N. A zonal transect along 4°N (Figure 7b) provides an explanation. Comparing Figure 7b with Figure 7a, one sees much more complex topographic structure south of 10°N, and the separation distances between ridges could provide wavelengths of choice for local internal tides. Several prominent meridional ridges reside between south of Palau and east of the Celebes Sea (Figure 1) and, not surprisingly, internal tide wavelengths are comparable to topographic wavelengths (∼100 km) in these regions (Figures 6 and 7b). A further dynamical investigation beyond the foregoing description is beyond the present scope but merits study.

4. Discussion

[16] The major feature of K$_1$ tide in the SCS is the twofold amplification, which leads to the predominance of diurnal over semidiurnal tides. Using the coamplitude and cophase patterns in Figure 4a as a guide, one can idealize

Figure 4. (a) Cotidal chart and (b) depth-averaged tidal current ellipses for the simulated K₁ tide. The open square AE at about (117°E, 22°N) in the top panel represents the study site of ASIAEX [*Lynch et al.*, 2004].

Figure 5. Observed [*Beardsley et al.*, 2004] and modeled K_1 barotropic tidal current ellipses at (a) five acoustic Doppler current profiler stations and (b) relative locations of the five stations in an area indicated by the square AE in Figure 4a.
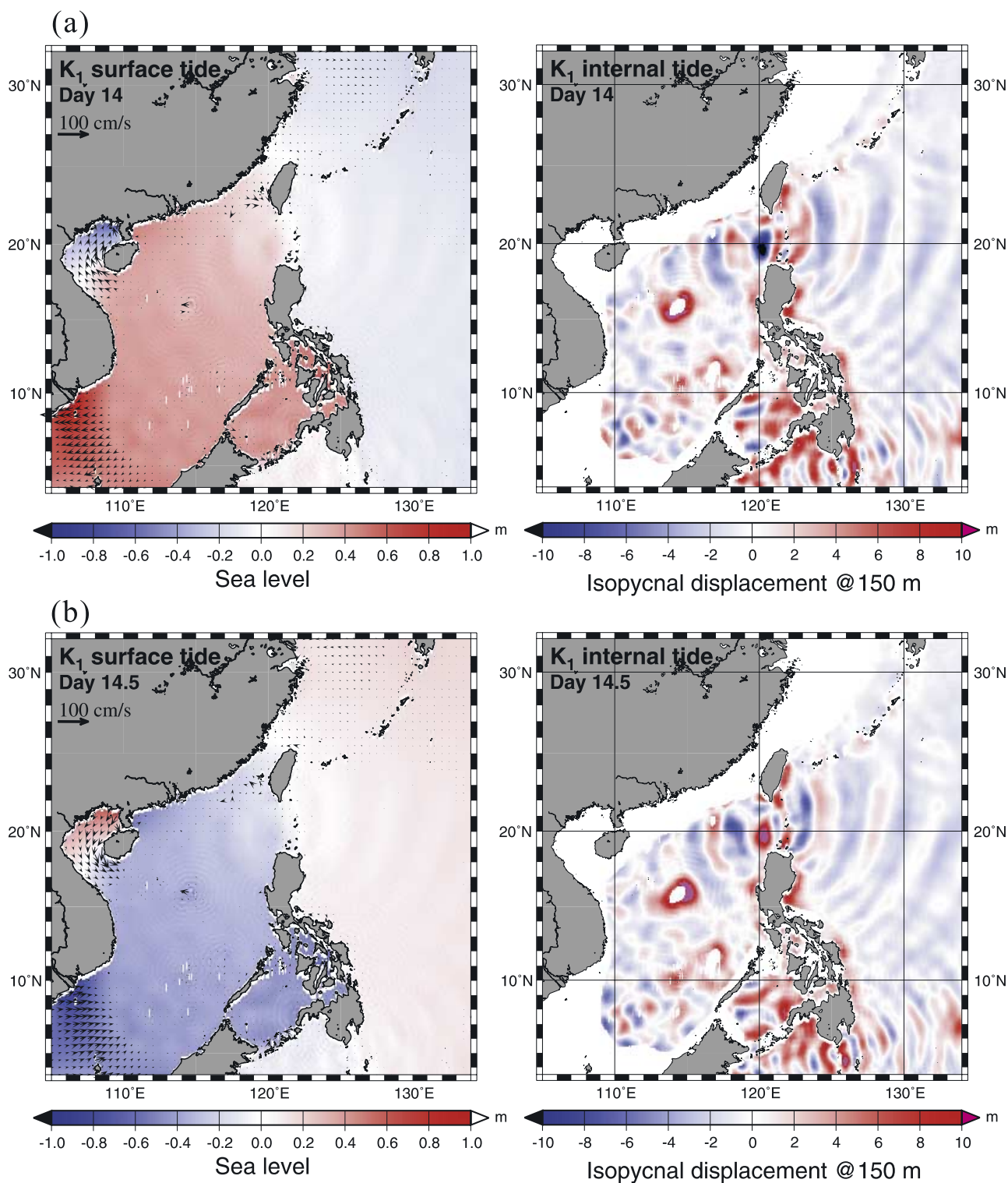
the setting for the following theoretical analysis. Imagine the SCS as a long and narrow channel with open ends at the Luzon Strait and over the Sunda Shelf. One can also idealize the shoaling bottom between the deep SCS basin and Sunda Shelf as a step-like topography with water depths of H_1 (~2000 m) over the former and H_2 (~100 m) over the latter. *Dean and Dalrymple* [1991] derived transmission and reflection coefficients of a linear frictionless long channel wave propagating over the step as $\kappa_t = \frac{2}{1+\sqrt{H_2/H_1}}$ and $\kappa_r = \frac{1-\sqrt{H_2/H_1}}{1+\sqrt{H_2/H_1}}$, respectively [section 5.5 in the book of *Dean and Dalrymple*, 1991]. Since $H_2 \ll H_1$, the reflection and transmission coefficients at the topographic step are approximately 0.7 and 1.7, respectively. Notably, the northward reflection from the Sunda Shelf causes the K_1 surface tide to behave as a partial standing wave in the central SCS. The behavior is consistent with our model results (section 3.1). Given a mean depth of 2000 m for the SCS, the wavelength of the barotropic K_1 tide (λ) is about 12,000 km. Fixing the antinode of the partial standing wave at the topographic step (Sunda Shelf), the Luzon Strait is about 3000 km or $\lambda/4$ away. Thus the SCS is close to being a quarter-wave resonator for K_1 tide with the Luzon Strait serving as a nodal point. The twofold amplification (20 cm in the Luzon Strait versus 40 cm in the SCS), small phase variation (~20°), and stronger tidal currents in the Luzon Strait are all indicative of quarter-wave resonance in the SCS. Moreover, the diurnal tide period is close to the first mode of free oscillation period of the SCS if one treats SCS as a harbor and Luzon Strait as the harbor mouth. Let L (~3000 km) be the distance between Luzon Strait and Karimata Strait and H (~2000 m) be the mean depth of SCS. The gravest mode of free oscillation period, $4L/(gH)^{1/2}$, is 23.8 hours, resulting in nearly resonant response of K_1 tide in the SCS.

[17] The resonant oscillation in an idealized rectangular harbor has been extensively studied both theoretically and experimentally in 1960s [e.g., *Miles and Munk*, 1961]. These studies essentially pointed out the sensitivity of wave behavior to the width of entrance and the incident wave condition. Since the internal tide generation in the Luzon Strait must extract tidal energy from the incident surface tide, it could in turn modify K_1 surface tide in the SCS to some extent. This subject is analytically intractable and has rarely been examined in literature. We analyze the energy budget from our model results below to address this issue.

[18] Following *Niwa and Hibiya* [2004], Table 2 lists essential formulae for calculating the barotropic and baroclinic tidal energy. Figure 8 shows depth-integrated barotropic energy flux, barotropic-to-baroclinic energy conversion rate, and baroclinic energy flux averaged over one K_1 tidal period. The distribution of barotropic energy flux in Figure 8a suggests that K_1 surface tide enters the SCS through the Luzon Strait and thereafter progresses southwestward. Table 3 summarizes the barotropic tidal energy budget in the SCS. The barotropic energy integrated along the east section of the Luzon Strait (122.5°E or L1 in Figure 8a) and north section of the Taiwan Strait (25°N or L2 in Figure 8a) is 34.2 GW (1 GW = 10^9 watt) westward and 0.6 GW southward, respectively. After propagating through the deep basin of SCS, the barotropic energy integrated along 10°N (L3 in Figure 8a) becomes 15.7 GW southward. Colors in Figure 8a indicate the barotropic-to-baroclinic energy conversion rate, which resides mostly in the Luzon Strait. We also find minor baroclinic energy conversion rate near Dongsha Island and over shallow reaches in the center and southeast of the SCS. The area-integrated barotropic-to-baroclinic energy conversion in the Luzon Strait (rectangular box in Figure 8a or 8b) is 12.4 GW, which is far greater than the similar conversion elsewhere in the SCS (1.0 GW in the vast area bounded by 10°N, 25°N, and the west boundary of Luzon Strait).

[19] The depth-integrated baroclinic energy flux in Figure 8b shows both westward and eastward propagation of K_1 internal tide energy in the Luzon Strait. Figure 8b also indicates some baroclinic energy generation near the island in central SCS and some northward reflection of baroclinic energy from islands in the southeastern SCS and northern edge of Sunda Shelf. The net outward baroclinic energy fluxes from Luzon Strait (rectangular box in Figure 8b) are 2.5 and 1.1 GW across the east and west sections, respec-
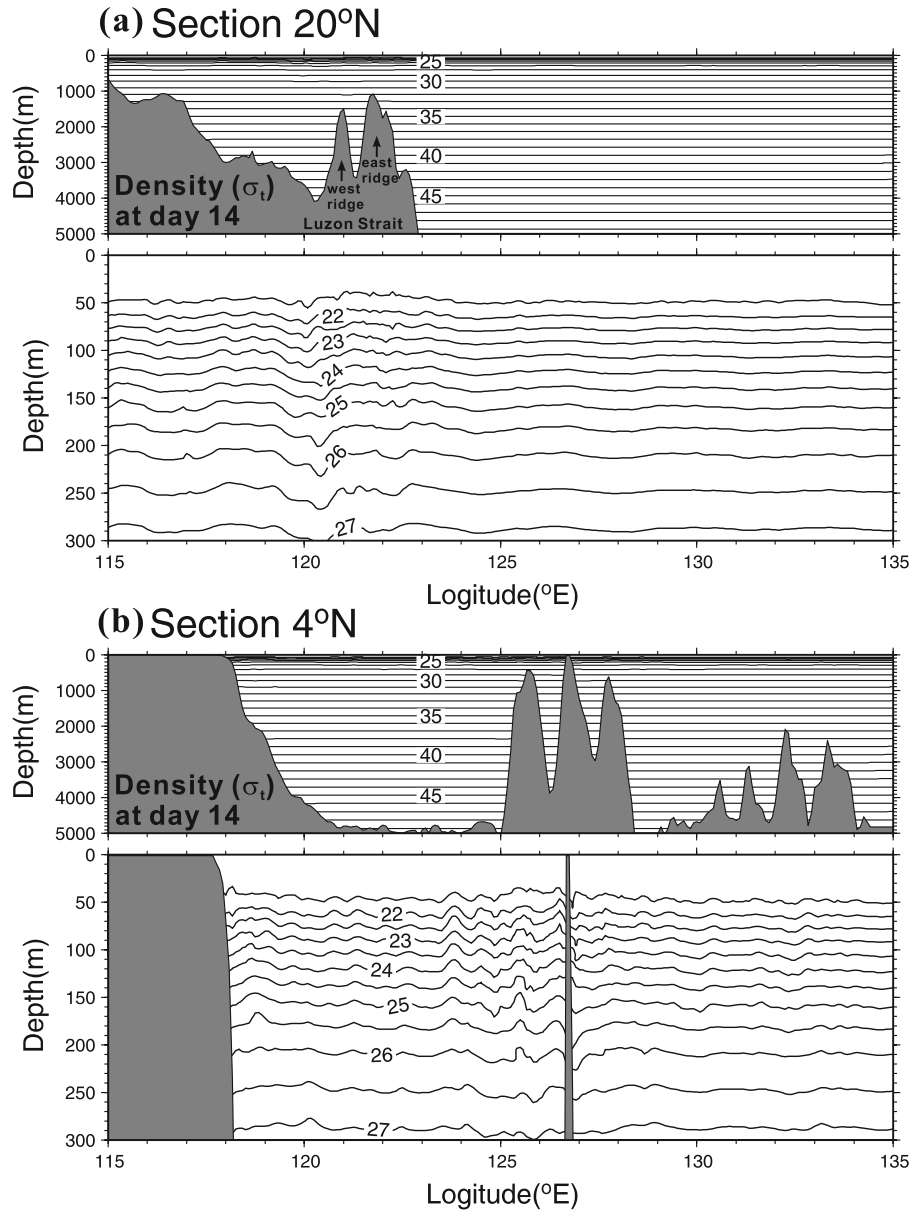
Figure 6. Instantaneous sea surface elevations (left panels) and vertical isopycnal displacements relative to 150 m depth (right panels) at (a) day 14 and (b) day 14.5. Also superimposed on left panels are instantaneous depth-averaged tidal currents.

tively. The estimation of the total energy budget indicates considerable barotropic energy ($\sim$5.6 GW) dissipation by bottom and lateral frictions in the SCS beyond 10°N and in the Luzon Strait. About 36% of the input barotropic energy is converted to the baroclinic energy for K$_1$ tide in the Luzon Strait. In comparison, similar conversion is only 25% for M$_2$ tide in the same region [*Niwa and Hibiya*, 2004].

[20] The aforementioned simulation is the control run. To assess the modification of K$_1$ surface tide caused by the 36% of barotropic energy loss to baroclinic energy in the
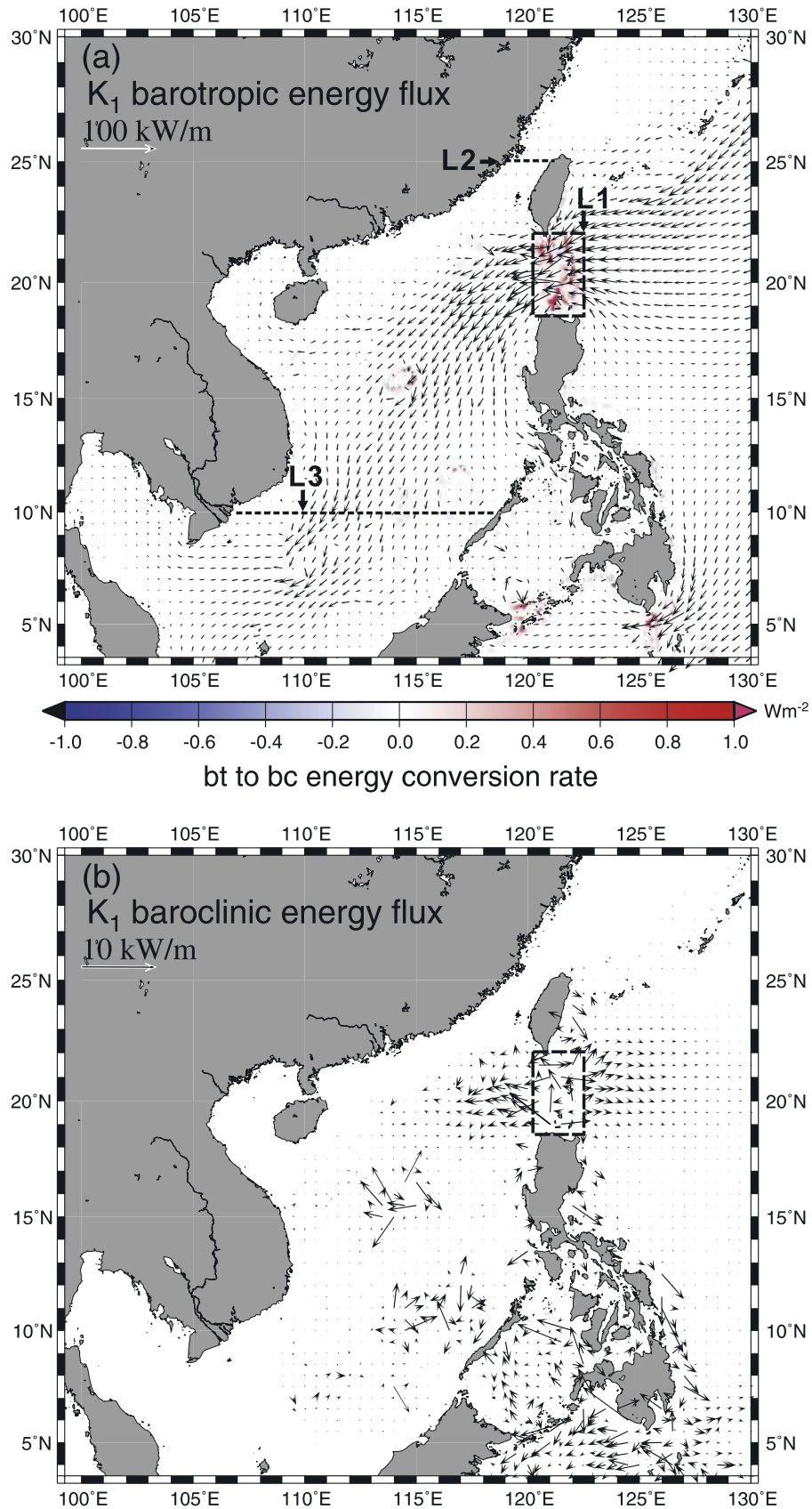
Figure 7. Instantaneous vertical density (σ_t) distribution and corresponding close-up of upper 300 m at day 14 along (a) 20°N and (b) 4°N.

Luzon Strait, five more numerical experiments with various stratification, topography, or sea level boundary condition are analyzed and discussed below. Table 4 lists the basic model configurations for control run and the five cases (A, B, C, and E). The ocean is homogeneous in cases A and B; case B assimilates observed sea level data but case A does not. In case B, sea level composed from harmonic constants of NAO.99 is assimilated into the model domain

Table 2. Formulae for the Calculation of Barotropic and Baroclinic Tidal Energy [*Niwa and Hibiya*, 2004]

Tidal Energy	Formulation
Depth-integrated barotropic energy flux in the x and y directions	$\left\langle \bar{U} \int_{-H}^{\eta} (g\rho_0(\zeta - \beta\eta) + P')\mathrm{d}z \right\rangle$ and $\left\langle \bar{V} \int_{-H}^{\eta} (g\rho_0(\zeta - \beta\eta) + P')\mathrm{d}z \right\rangle$, respectively, where ρ_0 represents the initial background density stratification, and angle brackets denote time average over one K$_1$ tidal period
Depth-integrated baroclinic energy flux in the x and y directions	$\left\langle \int_{-H}^{\eta} (U'P')\mathrm{d}z \right\rangle$ and $\left\langle \int_{-H}^{\eta} (V'P')\mathrm{d}z \right\rangle$, respectively, where (U', V') are the baroclinic velocity components in the x and y directions
Depth-integrated barotropic-to-baroclinic energy conversion rate averaged over one tidal period	$\left\langle g \int_{-H}^{\eta} \rho' w_{bt} \mathrm{d}z \right\rangle$, where $w_{bt} = \bar{U}\left(\sigma \frac{\partial D}{\partial x} + \frac{\partial \eta}{\partial x}\right) + \bar{V}\left(\sigma \frac{\partial D}{\partial y} + \frac{\partial \eta}{\partial y}\right) + \left(\sigma \frac{\partial \eta}{\partial t} + \frac{\partial \eta}{\partial t}\right)$ is the Cartesian vertical velocity relevant to the barotropic flow

Figure 8. (a) Depth-integrated barotropic energy flux and barotropic-to-baroclinic energy conversion rate and (b) baroclinic energy flux. All quantities are averages over one K_1 tide period.

Table 3. Barotropic Energy Budget of the Control Run in the SCS Bounded by Sections L1, L2, and L3 in Figure 8a[a]

Sectional BT Energy			BT-to-BC Energy Conversion Rate		Dissipations Due to Friction
L1	L2	L3	Luzon Strait	SCS	
+34.2	+0.6	−15.8	−12.4 (36% of L1)	−1.1	−5.6

[a]The L1, L2, and L3 (see Figure 8a for their locations) are sections to the east of the Luzon Strait, north of the Taiwan Strait, and south of the SCS, respectively. BT means barotropic while BC means baroclinic. Units are in GW.

in areas deeper than 2000 m according to the succeeding formula:

$$\eta = (1 - \varepsilon)\eta_{cal} + \varepsilon\eta_{NAO.99} \qquad (7)$$

where η_{cal} is the model-calculated sea level, $\eta_{NAO.99}$ is the sea level composed from harmonic constants of NAO.99, and $\varepsilon(= 0.15)$ is a constraint factor. In cases C, D, and E, the ocean is stratified as in the control run. In case C, both topographic ridges in the Luzon Strait are reduced by 50% in height relative to 3000 m depth. To distinguish the role of each ridge, the 50% height reduction is restricted to the west ridge (Hengchun Ridge) in case D and to the east ridge (Luzon Island Arc) in case E. Model results are discussed below.

[21] Figure 9 plots calculated harmonic constants along the major axis of the SCS (P-Q in Figure 4a) and a zonal section extending eastward from the Luzon Strait to the Pacific Ocean (Q-R in Figure 4a) for each case. Harmonic constants from NAO.99 are also plotted as a reference. As expected, the horizontal length scales of the fluctuations in amplitude and phase from the control run are close to the wavelengths of internal tides in the Pacific Ocean and the SCS. Similar modulation in the simulated barotropic M$_2$ tide has been verified by the comparison with TOPEX/ Poseidon altimeter data [*Niwa and Hibiya*, 2004]. Leaving oscillations induced by internal tides aside, all six simulations lead to harmonic constants close to NAO.99 on the Pacific Ocean side. On the SCS side, the results differ significantly from NAO.99 except for case B; this is understandable because case B assimilates NAO.99 into the model. The control run produces much smaller amplitude of harmonic constants than its homogeneous counterpart (case A) on the SCS side. Apparently, the energy-extracting internal tides in the Luzon Strait greatly reduce the amplitude of the simulated surface K$_1$ tide in the SCS. Without the barotropic-to-baroclinic energy conversion, the simulated amplitude is overestimated by 20–50% in the SCS. In other words, the amplification of surface K$_1$ tide caused by quasi-quarter-wave resonance is much reduced in the SCS due to the barotropic energy loss in the Luzon Strait. The ridge height reduction (in cases C, D, and E) also enhances the amplitude of K$_1$ surface tide on the SCS side because of reduced blocking and consequently reduced internal tide generation by the ridges. Without stratification (in cases A and B), the spatial variation of phase remains almost unchanged compared to that of NAO.99. With ridge height reduction in cases (C, D, and E), the K$_1$ surface tide propagates faster in the Luzon Strait because of the depth

increase. In consequence, the phase of transmitted wave in the SCS is advanced. The most severe ridge height reduction is case C, in which the phase is advanced by about 20° relative to NAO.99 in the SCS. Relative to case C, height reduction of either east ridge or west ridge causes smaller phase advance. East ridge reduction causes larger phase advance than does the west ridge reduction. This is conceivable because east ridge is, when averaged meridionally, higher than the west ridge and the consequent 50% height reduction is more severe. The close match between case B and NAO.99 points out the importance of data assimilation in tide prediction if one uses a tidal model without the generation of internal tides in the Luzon Strait.
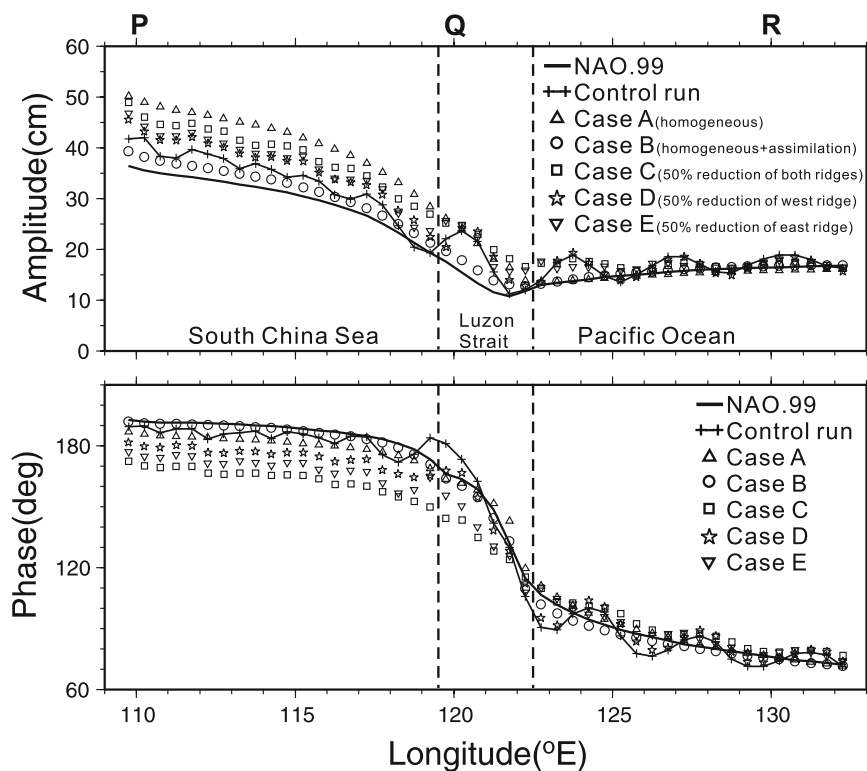
[22] Ridge height reduction not only reduces the barotropic-to-baroclinic energy conversion rate in the Luzon Strait but also changes the influx of barotropic tidal energy from the Pacific Ocean. In the control run, 36% (12.4 GW) of the barotropic influx from the Pacific Ocean (34.2 GW) is converted to baroclinic energy in the Luzon Strait (rectangular box in Figure 8a). The corresponding conversion rate is 27% (9.1 GW) of the barotropic influx (33.6 GW) in case D and 14% (6.7 GW) of the barotropic influx (47.2 GW) in case E. Apparently, east ridge height reduction (case E) decreases the barotropic-to-baroclinic conversion rate more because of the reason that it is the major ridge between the two. In other words, the east ridge in its present-day condition is the major source of internal K$_1$ tide in the SCS.

5. Concluding Remarks

[23] Entering the SCS, the K$_1$ barotropic tide becomes a partial standing wave in a near-resonance state. The generation of vigorous internal tides in the Luzon Strait thus considerably modifies the characteristic of the transmitted K$_1$ barotropic tide. With a typical summertime stratification of the SCS as the initial condition, model results indicate that the depth-integrated rate of the barotropic-to-baroclinic energy conversion amounts up to 36% of the K$_1$ barotropic tide energy influx (12.4 GW of 34.2 GW). The internal tides excited over the topographic ridges in the Luzon Strait propagate both eastward into the Pacific Ocean and west-southwestward into the SCS. Additional internal tides created over the shelf and slope regions in the southern SCS present wave interference pattern. Numerical experiments that eliminate or reduce the K$_1$ internal tide in the

Table 4. List of Numerical Experiments

Case	Initial Stratification	Sea Level Assimilation	Topographic Ridges in Luzon Strait
Control run	Typical SCS summer profile	No	Realistic
A	None	No	Realistic
B	None	Yes	Realistic
C	Typical SCS summer profile	No	50% reduction in height relative to 3000 m
D	Typical SCS summer profile	No	50% reduction in height relative to 3000 m for Heng-Chun Ridge only
E	Typical SCS summer profile	No	50% reduction in height relative to 3000 m for Luzon Island Arc only

Figure 9. Harmonic constants along P-Q-R section in Figure 4a from the control run and cases A, B, C, D, and E. Harmonic constants from NAO.99 are also plotted for comparison.

Luzon Strait further suggest that the baroclinic energy conversion reduces the amplitude of K$_1$ surface tide by about 30%. Our investigation also explains why a two-dimensional model without data assimilation or precisely prescribed sea levels around the Luzon Strait commonly overestimates amplitudes of diurnal tides in the SCS.

[24] The oceanographic condition around the Luzon Strait is far more complex than the present model setting. In this light, the influence of the seasonally varying Kuroshio on K$_1$ tide warrants further studies. Furthermore, the seasonal variation of the stratification in the SCS adds yet another complication to the generation of K$_1$ internal tide and the subsequent modification of K$_1$ surface tide; this also deserves future attention. More comprehensive field observations, especially on the Pacific Ocean side of Luzon Strait, are also needed for the validation of model results.

References

Beardsley, R. C., T. F. Duda, J. F. Lynch, J. D. Irish, S. R. Ramp, C.-S. Chiu, T.-Y. Tang, Y.-J. Yang, and G. Fang (2004), Barotropic tide in the northeast South China Sea, *IEEE J. Oceanic Eng.*, 29(4), 1075–1086.

Blumberg, A. F., and L. H. Kantha (1985), Open boundary condition for circulation models, *J. Hydraul. Eng.*, 111(2), 237–255.

Blumberg, A. F., and G. F. Mellor (1987), A description of a three-dimensional coastal ocean circulation model, in *Three-Dimensional Coastal Ocean Models, Coastal and Estuarine Sciences*, vol. 4, edited by N. Heaps, pp. 1–16, AGU, Washington, D. C.

Chen, C.-C., F.-K. Shiah, S.-W. Chung, and K.-K. Liu (2006), Winter phytoplankton blooms in the shallow mixed layer of the South China Sea enhanced by upwelling, *J. Mar. Syst.*, 59, 97–110, doi:10.1016/j.jmarsys.2005.09.002.

Clarke, A. J. (1991), The dynamics of barotropic tides over the continental shelf and slope (review), in *Tidal Hydrogynamics*, edited by B. Parker, 79–108, John Wiley, Hoboken, N. J.

Dean, R. G., and R. A. Dalrymple (1991), Water wave mechanics for engineers and scientists: Section 5.5. Reflection and transmission past an abrupt transition, pp. 141–144 (353 pp), Scientific Gainesville, Fla.

Duda, T. F., J. F. Lynch, J. D. Irish, R. C. Beardsley, S. R. Ramp, C.-S. Chiu, T.-Y. Tang, and Y.-J. Yang (2004), Internal tide and nonlinear internal wave behavior at the continental slope in the northern South China Sea, *IEEE J. Oceanic Eng.*, 29(4), 1105–1130.

Engedahl, H. (1995), of the flow relaxation scheme in a three-dimensional baroclinic ocean model with realistic topography, *Tellus Ser. A*, 47, 365–382.

Fang, G., Y.-K. Kwok, K. Yu, and Y. Zhu (1999), Numerical simulation of principal tidal constituents in the South China Sea, Gulf of Tonkin and Gulf of Thailand, *Cont. Shelf Res.*, 19, 845–869.

Foreman, M. G. G., R. F. Henry, R. A. Walters, and V. A. Ballantyne (1993), A finite element model for tides and resonance along the north coast of British Columbia, *J. Geophys. Res.*, 98, 2509–2532.

He, R., and R. H. Weisberg (2002), Tides on the west Florida shelf, *J. Phys. Oceanogr.*, 32, 3455–3473.

Huang, Q., W. Wang, and J. Chen (1994), Tides, tidal currents and storm surge set-up of South China Sea, in *Oceanology of China Seas*, vol. 1, 113–122, edited by Zhou, D., et al., Springer, New York.

Jan, S., C.-S. Chern, J. Wang, and S.-Y. Chao (2004), The anomalous amplification of M$_2$ tide in the Taiwan Strait, *Geophys. Res. Lett.*, 31, L07308, doi:10.1029/2003GL019373.

Lynch, L. F., S. R. Ramp, C.-S. Chiu, T.-Y. Tang, Y.-J. Yang, and J. A. Simmen (2004), Research highlights from the Asian Seas International Acoustics Experiment in the South China Sea, *IEEE J. Oceanic Eng.*, 29(4), 1067–1074.

Matsumoto, K., T. Takanezawa, and M. Ooe (2000), Ocean tide models developed by assimilating TOPEX/POSEIDON altimeter data into hydro-dynamical model: A global model and a regional model around Japan, *J. Oceanogr.*, 56, 567–581.

Mazzega, P., and M. Berge (1994), Ocean tides in the Asian semienclosed seas from TOPEX/POSEIDON, *J. Geophys. Res.*, 99(C12), 24,867–24,881.

Mellor, G. L. (2004), Users guide for a three-dimensional, primitive equation, numerical ocean model. http://www.aos.princeton.edu/WWWPUBLIC/htdocs.pom/

Mellor, G. L., and T. Yamada (1982), Development of turbulence closure model for geophysical fluid problems, *Rev. Geophys.*, *20*, 851–875.

Miles, J., and W. Munk (1961), Harbor paradox, *J. Waterw. Harb. Div.*, *87*(3), 111–130.

Niwa, Y., and T. Hibiya (2001), Numerical study of the spatial distribution of the M2 internal tide in the Pacific Ocean, *J. Geophys. Res.*, *106*, 22,441–22,449.

Niwa, Y., and T. Hibiya (2004), Three-dimensional numerical simulation of M₂ internal tides in the East China Sea, *J. Geophys. Res.*, *109*, C04027, doi:10.1029/2003JC001923.

Pugh, D. T. (1987), Tides, surges and mean sea-level, John Wiley, 471 pp., Hoboken, N. J.

Ramp, S. R., T.-Y. Tang, T. F. Duda, J. F. Lynch, A. K. Liu, C.-S. Chiu, F. L. Bahr, H.-R. Kim, and Y.-J. Yang (2004), Internal solitons in the northeastern South China Sea: Part I. Sources and deep water propagation, *IEEE J. Oceanic Eng.*, *29*(4), 1157–1181.

Reid, R. O., and R. E. Whitaker (1981), Numerical model for astronomical tides in the Gulf of Mexico, *Texas A&M Rep. for U.S. Army Engineers Waterway Experiment Station*, 115 pp.

Smagorinsky, J. S. (1963), General circulation experiments with the primitive equations: I. The basic experiment, *Mon. Weather Rev.*, *91*, 99–164.

U.S. Department of Commerce, National Oceanic and Atmospheric Administration, and National Geographic Data Center (2001), Two-minute Gridded Global Relief Data (ETOPO2). http://www.ngdc.noaa.gov/mgg/flier/01mgg04.html)

Yanagi, T., T. Takao, and A. Morimoto (1997), Co-tidal and co-range charts in the South China Sea derived from satellite altimetry data, *La mer*, *35*, 85–94.

Yanagi, T., and T. Takao (1998), A numerical simulation of tides and tidal currents in the South China Sea, *Acta Oceanogr. Taiwan.*, *37*(1), 17–29.

Ye, A. L., and I. S. Robinson (1983), Tidal dynamics in the South China Sea, *Geophys. J. R. Astron. Soc.*, *72*, 691–707.

Zetler, B. D., and D. V. Hansen (1971), Tides in the Gulf of Mexico, Contributions on the Physical Oceanography of the Gulf of Mexico, edited by L. R. A. Capurro and J. L. Reid, vol. 2, pp. 265–275, Gulf, Houston, Tex.

_____

S.-Y. Chao, Horn Point Laboratory, University of Maryland Center for Environmental Science, P.O. Box 0775, Cambridge, MD 21613-0775, USA.

C.-S. Chern and J. Wang, Institute of Oceanography, National Taiwan University, P. O. Box 23-13, Taipei 10617, Taiwan, Republic of China.

S. Jan, Institute of Hydrological Sciences, National Central University, 300 Jung-da Road, Jung-li 32001, Taiwan, Republic of China. (senjan@cc.ncu.edu.tw)